UNIVERSITY OF SOUTHAMPTON

Faculty of Engineering and Physical Sciences

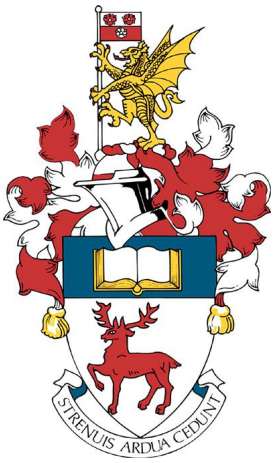

Flexible Sheets in Turbulent Flow

by

Marin Lauber

Supervised by:
Dr. G.D. Weymouth
&
Dr. G. Limbert

First Progression Review – Month 9

September 2020

Contents

List of Figures

List of Tables

1 Introduction

Fluid-structure interaction is concerned with the coupled motion of a solid immersed in a fluid; this encompasses a wide range of phenomenon: from the fluttering of leaves on a windy day to the violent aerodynamic loads encountered by an airplane wing. In these cases, pressure and viscous forces from the fluid are reacted by internal stresses in the solid. These internal stresses result in topological changes of the solid, which influence the flow of fluid and thus the forces. This fundamental concept of coupling of both systems is one of the major challenges that make this kind of problem laborious to treat.

In some cases, it is possible to make some simplification regarding the coupling, but in the most general case, these assumptions would introduce significant errors.

One such approximation is the rigid body approach, where we consider the solid as static relative to the fluid. This assumption is valid when the typical time-scale of the fluid is much smaller than the typical time-scale of the body (de Langre et al., 2016). Typical examples are the flow around a circular cylinder or an airplane's wing. In these cases, the deformation of the solid is relatively small and occurs at a time scale much larger than that of these high Reynolds number flows.

However, a large portion of fluid-structure interaction systems do not fall in this category, for examples; leaves fluttering, parachute inflation or the motion of a kite on a sailboat. All these systems consist of a thin elastic structure that interacts with the surrounding fluid. Here the time-scale of both system is of the same order, and the rigid body approximation becomes erroneous. Also, the low rigidity (large Cauchy number) and mass of the structure can introduce large non-linear deformation and significant added-mass effects (Causin et al., 2005).

Numerical simulation of those systems is a complex task, for several reasons; the large structural deformations require numerical methods that allow large body motion and deformation, while still being computationally efficient. High Reynolds number flow requires high-resolution numerical methods to capture all the fine spatial and temporal scales of the flow. Sophisticated non-linear methods are required to solve the structural mechanic problem due to the geometrical (and possibly material) non-linearity. Finally, the coupling method must be robust enough the accommodate small mass ratios (ρ_s/ρ) and the associated added-mass effect. Numerous examples of various complexities have been presented for applications ranging from aortic valve simulations (Y. Chen and H. Luo, 2018; Gilmanov et al., 2015; Tullio and Pascazio, 2016), for which the immersed boundary method was developed, to parachute inflation (Karagiozis et al., 2011; Yu et al., 2019) where Large-Eddy-Simulation (LES) methods are coupled with shell-elements to model the parachute dynamics. Downwind sail simulations usually prefer less advanced numerical methods (RANS) where viscous, and pressure forces are communicated to the structural model only a couple of time (Platon, 2011; Renzsch and Graf, 2014; Richter et al., 2003) to get the flying shape of the kite. Others simulations used strongly coupled algorithms

(Ramolini, 2019) to model more accurately the complex interaction of the sail. Trimarchi et al. (2010) investigated the effect of sail wrinkling on the aerodynamics of downwind sail using a strongly-coupled FSI model with a structural resolution able to capture most of the wrinkles and fold in the kite. With some more advanced fluid models (URANS) (Lombardi et al., 2012) detailed kite dynamics during a broach have been investigated. However, this study showed the limitations of body-fitted approaches when the simulations stopped once the structural deformation was too large. Biological FSI is also an area of active research for complex fluid-structure interaction simulations of three-dimensional flapping wings (Bos et al., 2013; Wang et al., 2004; Zheng et al., 2020) or fish fins (Y. Luo et al., 2020).

This thesis aims at developing a numerical model for simulating the interaction of flexible sheets/membranes with an unsteady (potentially turbulent) flow. The method must be able to accommodate arbitrary large displacement, without large computational overheads and be robust enough to work for a wide range of mass-ratios. This allows us to split this thesis into three distinct parts; the first part must deal with accommodating important structural displacement in the fluid domain, the second part deals with the structural mechanics required to model those thin structures and finally, the last part treats of the coupling between those two systems.

This report is structure as follow; section 2 introduces the coupled fluid-structure interaction system more rigorously and describes the boundary conditions and the numerical solution to this system. Section 3 focuses on the Cartesian grid methods and the associated issues that are ubiquitous with thin structures. We also introduce a uni-dimensional fluid-structure interaction problem that allows demonstrating all the concepts presented in the preceding sections. Finally, section 4 provides a look into the future steps of this project and concludes this report.

2 The Coupled Fluid-Structure Interaction System

2.1 Governing Equations and Boundary Conditions

The general fluid-structure interaction problem considers an domain $\Omega^t \subset R^d$ $(d = 2, 3)$ with t spanning the interval of analysis $[0, T]$. The domain is divided into a solid Ω_s^t and a fluid part Ω_f^t. The fluid-structure interface Σ^t is the boundary of the solid and the fluid i.e. $\partial\Omega_s^t \cap \partial\Omega_f^t$. This is the most general fluid-structure interaction system, in our case, we restrict ourselves of a solid having one dimension less than the fluid, i.e. the fluid domain now contains an interface Γ^t, which is the domain of the solid.

In addition, we will restrict our attention to incompressible flows governed by the Navier-Stokes equations

$$\begin{aligned} &\frac{\partial \boldsymbol{u}}{\partial t} + (\boldsymbol{u} \cdot \nabla)\boldsymbol{u} - \frac{1}{\rho_f}\nabla \cdot \sigma^f = \boldsymbol{f}_f \qquad \text{in } \Omega_f^t \times (0, T), \\ &\nabla \cdot \boldsymbol{u} = 0 \qquad \text{in } \Omega_f^t \times (0, T), \end{aligned} \tag{2.1}$$

where $\boldsymbol{u}$ is the fluid velocity, σ^f the Cauchy stress tensor and $\boldsymbol{f}$ a body force. For a Newtonian fluid the Cauchy stress tensor take a simple form

$$\sigma^f(\boldsymbol{u}) = -pI + 2\mu\varepsilon(\boldsymbol{u}), \tag{2.2}$$

with I the identity tensor and $\varepsilon(\boldsymbol{u})$ the strain rate tensor

$$\varepsilon(\boldsymbol{u}) = \frac{1}{2}\left(\nabla \boldsymbol{u} + (\nabla \boldsymbol{u})^\top\right). \tag{2.3}$$

The solid is governed by the elastodynamic equations

$$\frac{\partial^2 \boldsymbol{\xi}}{\partial t^2} - \frac{1}{\rho_s}\nabla \cdot \sigma^s = \boldsymbol{f}_s \qquad \text{in } \Gamma_s^t \times (0, T). \tag{2.4}$$

This equation must be supplemented with a constitutive law that relates the structural displacements $\boldsymbol{\xi}$ to the Cauchy stress tensor σ^s, for example the linear Saint-Venant Kirchhoff 3D model

$$\sigma^s(\boldsymbol{\xi}) = 2\mu_l\varepsilon(\boldsymbol{\xi}) + \lambda_l(\nabla \cdot \boldsymbol{\xi})I, \tag{2.5}$$

where μ_l and λ_l are Lame constants.

The two problems are coupled at the interface by a Dirichlet condition on the velocities (np-slip/no-penetration)

$$\boldsymbol{u} = \frac{\partial \boldsymbol{\xi}}{\partial t} \qquad \text{on } \Gamma^t \times (0, T). \tag{2.6}$$

and a Neumann condition on the stresses (continuity of stresses)

$$\sigma^s \cdot \hat{n} = \sigma^f \cdot \hat{n} \qquad \text{on } \Gamma^t \times (0,T) \tag{2.7}$$

where $\hat{n}$ is the unit normal vector of the solid. This last equation is only valid in the case of an elastic solid, where stresses must balanced, if the solid is considered as rigid, the only condition at the interface is (2.6).

The dynamic boundary condition is obtained by projecting the conservation of momentum on a vector normal to the interface

$$\hat{n} \cdot \left[\frac{\partial \boldsymbol{u}}{\partial t} + (\boldsymbol{u} \cdot \nabla)\boldsymbol{u} = -\frac{1}{\rho}\nabla p + \nu \nabla^2 \boldsymbol{u} \right]. \tag{2.8}$$

With proper non-dimensionalisation of the equation, this can be rewritten as

$$-\hat{n} \cdot \nabla p = -\left(\frac{\partial p}{\partial n} \right) = \hat{n} \cdot \left[St \frac{D\boldsymbol{u}}{Dt} - \frac{1}{Re}\nabla^2 \boldsymbol{u} \right]. \tag{2.9}$$

For sufficiently large Reynolds numbers, the expression simplifies to

$$-\left(\frac{\partial p}{\partial n} \right) = St \left[\hat{n} \cdot \frac{\partial \boldsymbol{V}}{\partial t} \right], \qquad \text{on } \Gamma^t \times (0,T) \tag{2.10}$$

Here we have substituted the Lagrangian acceleration of the body in place of the Eulerian acceleration of the fluid. The standard homogeneous pressure boundary condition is recovered in the case of a stationary or steadily moving body.

2.2 Numerical Solution to the Coupled FSI Problem

Numerical solutions to the coupled fluid-structure interaction problems can be obtained using two different classes of algorithms. Monolithic approaches use the same discretization for the solid and the fluid. This can result in very efficient algorithms but their robustness is not excellent. Alternatively, one can use specialized methods for each system and couple them through the boundary conditions; this is the partitioned approach. It is widely used for fluid-structure interaction problem as is allows *back-box* solvers to be used and allows for great flexibility while requires minimal implementation compared to the monolithic approach.

In partitioned algorithms, each system of the coupled fluid-structure interaction problems are solved separately and coupled through the boundary conditions. Partitioned algorithms are classified into weakly and strongly coupled algorithms. Weakly-coupled algorithms perform a single iteration between the two systems, resulting in approximate equilibrium. Strongly-coupled partitioned algorithms iterate until it reaches a given tolerance. This makes strongly coupled algorithms much more computationally expansive. However, some applications require that the

equilibrium is satisfied accurately to give relevant results.

Partitioned approaches usually rely on a body-fitted discretization of the fluid domain, which allows trivial imposition of the boundary condition. Two widely used methods are the Arbitrary Lagrangian-Eulerian (ALE) and space-time method (Bazilevs et al., 2013). The Arbitrary Lagrangian-Eulerian (ALE) method has been the method of choice for some time. This method allows precise control of mesh resolution close the body while being very efficient at imposing boundary condition on the interface between the solid and the fluid. However, it suffers from low accuracy and computational inefficiency when large deformations have to be accommodated or when the mesh resolution required near the body is too fine. These large cell deformations result in low accuracy in areas where high accuracy would be required (close to the body). Besides, the re-meshing and the unstructured solver required are computationally inefficient. For linear fluid-structure interaction problems or problems where an efficient re-meshing strategy is available, those methods are unmatched in terms of accuracy. However, for the type of problems where our interest lies, those methods are not expected to perform well.

Cartesian methods are an attractive alternative for this kind of systems, by solving the equation on a static background mesh, large structural deformation can now be accommodated, at the cost of being less trivial in imposing boundary conditions. The next chapter will detail a range of numerical methods used to impose those boundary conditions. Kim and Choi (2019) provide a detailed review of immersed boundary methods for fluid-structure interaction.

3 Cartesian Grid Methods

We will use the term Cartesian grid methods to enclose all methods that use a discretization of the fluid domain that do not conform to the immersed body. Numerous methods have been proposed since those types of methods were first derived by Charles S Peskin (1972). While the original method used a finite-difference discretization of the fluid equation, Cartesian grid methods have been proposed for the finite-volume, finite-element and even spectral methods (Jause-Labert et al., 2012). The finite volume method is extensively used for fluid simulation, mostly because of some good conservation properties (energy and momentum) that are not found in other methods. Regardless, the different Cartesian methods are usually extendable to other discretization strategies.

Cartesian grid methods aim at solving the coupled system of equations on a background grid that do not conform to the body. By doing so, a wide range of structural displacement can be accommodated; however, elaborated treatment of the boundary conditions are required as grid points do not coincide with the position of the body. Perhaps the most straightforward way of solving this issue is to reshape the cells cut by the interface (cut-cell method). Cut cells require a different treatment of the convective flux (Xie and Stoesser, 2020)

$$\iint_S (\rho \boldsymbol{u} \cdot \boldsymbol{n}) \varphi \, \mathrm{d}S = \sum_f (\rho \boldsymbol{u} \cdot \boldsymbol{n} \theta A)_f \varphi_f, \tag{3.1}$$

where θ and A are the cut-cell availability function[1] and area of the cell face f. The diffusive fluxes are evaluated in a similar manner

$$\iint_S \Gamma \frac{\partial \varphi}{\partial n} \, \mathrm{d}S = \sum_f \Gamma_f \frac{\partial \varphi}{\partial n} (\theta A)_f + \tau_w [(1-\theta)A]_f, \tag{3.2}$$

where τ_w is (the prescribed) wall shear stress. Computation of those modified flux (through $(\theta A)_f$) is not straightforward as the exact geometry of the cut cell must be known. In 3D, this is a cumbersome task, as many different cut-cells can be generated. Also, small cut-cells result in numerical instabilities that require special treatments, such as implicit schemes (Xie and Stoesser, 2020), modifying the control volumes through cell merging or the use of a flux re-distribution scheme. Additional complications arise for interface-like structures, here the cell cut by the interface results in a new cell being generated, and convective and diffusive fluxes have to be computed and stored for these two cells. Apart from the finite volume method, discontinuous Galerkin methods also extensively use the cut-cell method for Cartesian grid simulations, see Xiao et al. (2019).

[1] This function take the value 1 if the face is available and 0 if not.

Charles S Peskin (1972) developed the immersed boundary method (IBM) to tackle the problem of heart valves. Dirac delta function source terms impose the kinematic boundary condition in the fluid by regularizing a force density on the background mesh

$$\frac{\partial \boldsymbol{u}}{\partial t} + (\boldsymbol{u} \cdot \nabla)\boldsymbol{u} = -\frac{1}{\rho}\nabla p + \nu \nabla^2 \boldsymbol{u} + \int_s \boldsymbol{F}(\boldsymbol{\xi}(s,t))\delta(\boldsymbol{\xi} - \boldsymbol{x})\,\mathrm{d}s. \tag{3.3}$$

A constitutional relationship, Hooke's law, is used to derive this force density based on the motion of the filament, convected by the fluid

$$\boldsymbol{F}(\boldsymbol{\xi}(s,t)) = -\frac{\partial E}{\partial \boldsymbol{\xi}}. \tag{3.4}$$

While this method works well for very elastic structures, it requires artificially large stiffness terms to model rigid structures. Additionally, when a fractional step approach is used to solve the system of coupled equations the kinematic boundary condition is only imposed on the intermediate velocity field, this results in an approximate imposition of the boundary condition after the corrector step. While this error is said to be small, it is hard to properly evaluate its magnitude. This results in leakage through the membrane when it separates region with different pressure magnitude (as it occurs in ventricular systole). Divergence-free force density terms (Bao et al., 2017; Charles S. Peskin and Feller Printz, 1993) remove this error but require more complex variables to be stored (cell edge vector potential). This also improves mass conservation when closed solid are simulated, but requires modification of the fluid's density surrounding the solid to simulate structures with mass (McQueen et al., 2007). Also, only formally second-order immersed boundary methods have been derived, see Lai and Charles S. Peskin (2000). This means that the second-order behaviour is obtained only when the discrete Dirac delta function is replaced with smooth function, independently of the mesh, which does not happen in practice.

For rigid structures, Goldstein et al. (1993) developed a feedback-forcing method that uses an integral controller to drive the fluid to the correct boundary condition close to the body

$$\boldsymbol{F}(\boldsymbol{\xi}(s,t)) = \alpha_f \int_0^t [u(\boldsymbol{\xi}(s,t)) - V(\boldsymbol{\xi}(s,t))]\,\mathrm{d}t' + \beta_f [u(\boldsymbol{\xi}(s,t)) - V(\boldsymbol{\xi}(s,t))], \tag{3.5}$$

where $V(\boldsymbol{\xi}(s,t))$ is the velocity of the solid in the local coordinate system. α_f and β_f are negative constants, which have a strong influence on the stability of the calculations. Numerous other types of forcing have been derived, see the reviews from Huang and F. B. Tian (2019) and Mittal and Iaccarino (2005) for examples.

Bale et al. (2020) recognised that for thin immersed bodies, the pressure jump across the interface is very badly capture by standard discretization schemes, they introduced a correction terms to the Dirac forcing that correct for the bad approximation obtained around this discontinuity

$$\boldsymbol{f}(\boldsymbol{x},t) = \boldsymbol{f}_{ct}(\boldsymbol{x},t) + \boldsymbol{f}_p(\boldsymbol{x},t) \tag{3.6}$$

where $\boldsymbol{f}_p(\boldsymbol{x}, t)$ is the correction term to account for the bad approximation of the pressure gradient obtain from central difference (or similar) schemes. This term is obtained form

$$\boldsymbol{f}_p(\boldsymbol{x}, t) = \nabla p - \hat{\nabla} p, \tag{3.7}$$

where $\hat{\nabla}$ is the modified gradient operator that penalises stencil that contain a jump in the pressure such that they are not used. WENO smoothness indicators are used to penalize the stencils close to the interface. The additional forcing term is thus only active near the interface. The final velocity field us the obtained

$$\boldsymbol{u}^{n+1} = \boldsymbol{u}^* - \frac{\Delta t}{\rho}(\nabla p - \boldsymbol{f}_p) \tag{3.8}$$

where the pressure p is obtained by solving a modified pressure correction equation

$$\nabla \cdot (\nabla p) = \frac{\rho}{\Delta t} \nabla \cdot \boldsymbol{u}^* + \nabla \cdot \boldsymbol{f}_p. \tag{3.9}$$

This approach is termed Stencil Penalty based Constraint IB (SPcIB) and has shown some improvements over the standard immersed boundary method. While this solves the problem of approximating a gradient across a discontinuity, it does not help in enforcing the correct boundary conditions on the pressure during the projection step.

While immersed boundary method provide some sort of Dirac delta forcing term to drive the fluid to the correct velocity, Direct forcing methods explicitly provide a forcing term that drives the fluid to the correct velocity inside the body

$$\frac{\partial \boldsymbol{u}}{\partial t} + (\boldsymbol{u} \cdot \nabla)\boldsymbol{u} = -\frac{1}{\rho}\nabla p + \nu \nabla^2 \boldsymbol{u} + \boldsymbol{f} \tag{3.10}$$

where the forcing is defined as

$$\boldsymbol{f} = \begin{cases} (\boldsymbol{u} \cdot \nabla)\boldsymbol{u} - \frac{1}{\rho}\nabla p + \nu \nabla^2 \boldsymbol{u} + \frac{\boldsymbol{V} - \boldsymbol{u}}{\Delta t} & \text{in } \Omega_b, \\ 0 & \text{in } \Omega_f. \end{cases} \tag{3.11}$$

which ensures that $\boldsymbol{u}^{n+1} = \boldsymbol{V}$ in the solid. First- and second-order methods have been derived by treating the cell partially cut by the solid with different interpolation schemes (Fadlun et al., 2000). However, this method is often used within a projection method and the resulting final velocity field does not fully satisfies the boundary condition. As we will show later, this is a flaw that is common to many immersed boundary method; correct kinematic boundary conditions are imposed on the intermediate velocity field, but because the pressure projection step is left unchanged by the immersed body, the resulting velocity field does not satisfies this condition anymore.

Ghost cell methods are an extension of ghost fluid methods methods (Fedkiw et al., 1999) originally developed for sharp interface multi-phase flows. An extra layer of cells, termed *ghost cells*, are added behind the boundary for each phase. The value of those ghost cells is chosen such that the correct boundary conditions are obtained at the interface between the two fluid. Ghost cells method use this layer of *ghost cells* to impose the kinematic boundary conditions. Because grid points do not usually align with the interface, the flow field variable have to be reconstructed normal to the interface before the ghost cells can be populated. Level-set functions are usually used with ghost-cells to provide an efficient representation on the interface

$$\boldsymbol{x}_{MP} = \boldsymbol{x}_{XG} + \frac{\nabla\phi}{\|\nabla\phi\|}|\phi|, \tag{3.12}$$

where ϕ is the level-set function and $\boldsymbol{x}_{MP}$ is the mirror point used to interpolate the ghost value from the known boundary condition at $\boldsymbol{x}_{XG}$. Depending on the location of the mirror point, different strategies have to be used to reconstruct the field variable from neighbouring nodes (Xin et al., 2018). The number of ghost cells required inside the body depends on the order of the interpolation used and the discretization. Zeng and Farhat (2012) derive a method to satisfy the kinematic boundary condition up to arbitrary order.

Ghost cells methods have been extensively used with the Euler equations (Cirak and Radovitzky, 2005; Karagiozis et al., 2011; Vanna et al., 2020). Here the ghost cell are directly provided with the vector of conservative variable $\boldsymbol{u} \equiv [\rho, \rho u_i, \rho E]^\top$, whereas compressible flow would require solving an elliptical equation to determine the pressure (up to a constant). To ensure that the correct boundary condition are imposed on the pressure, explicit modification of the Laplacian matrix is required on the internal boundaries (Chi et al., 2020; Ghias et al., 2007). Ghost-cells methods are known to produce pressure oscillations when nodes initially inside the body find move outside of it. One way to deal with those pressure oscillations is to add a mass source/sink in cells freshly cleared by the body (Xin et al., 2018).

The issue of bad gradient approximation for discontinuous variables was recognized by Lee and LeVeque (2003) and LeVeque and Li (1994) who developed the immersed interface method (IIM). Because of the discontinuity of certain fluid properties across the immersed interface, standard Taylor series expansions do not converge. However, if the jump of quantities across the interface is known, modified Taylor series expansions can be written and correction terms that account for those discontinuities can be added to the system of algebraic equations. By relating those discontinuities to properties of the problem to be solved (or Peskin-like volumetric forcing) discontinuous solutions can be obtained. These correction terms manifest themselves as additional source term on the right-hand-side of the pressure Poisson equation

$$\nabla \cdot \frac{1}{\rho}\nabla p = \nabla \cdot \boldsymbol{u} + \int_\Omega \boldsymbol{f_n} \nabla \cdot \delta(\boldsymbol{\xi} - \boldsymbol{x}) \, \mathrm{d}\boldsymbol{x}. \tag{3.13}$$

Which effectively modifies the discretization of the pressure Laplacian by accounting for the

known jump quantities across the interface. This effectively replace the discrete dipole in the intermediate step by providing a more accurate estimate of this singularity by modifying the pressure-projection equation. Expressions for f_τ and f_n can be obtained analytically from the boundary conditions on the immersed interface

$$\begin{aligned} [\![p]\!] &= f_n, \\ [\![u]\!] &= 0, \\ [\![p_{,n}]\!] &= \partial_s f_\tau, \\ [\![u_{,n}]\!] &= -f_\tau \tau, \end{aligned} \tag{3.14}$$

where s is the arc length used to parametrize the interface. Once those jumps are known, solution to the discontinuous problem is straight-forward, however in the general fluid-structure interaction problem, the jumps are the unknowns. The normal and tangential components of a Peskin-type forcing or penalty methods (Kolahdouz et al., 2020) can also be used instead of the correct jump conditions, but this only slightly improve the results obtained with the standard IBM (Lee and LeVeque, 2003).

Colonius and Taira (2008) and Taira et al. (2007) recognized that Peskin's volumetric forcing can be seen as another Lagrange multiplier (the first one being the pressure in an incompressible flow) that ensures that the kinematic boundary condition is satisfied. This means that the three momentum equations, along with two constrain equations are solved simultaneously

$$\begin{aligned} &\frac{\partial \boldsymbol{u}}{\partial t} + (\boldsymbol{u}\cdot\nabla)\boldsymbol{u} = -\frac{1}{\rho}\nabla p + \nu\nabla^2\boldsymbol{u} + \int_s \boldsymbol{f}(\boldsymbol{\xi}(s,t))\delta(\boldsymbol{\xi}-\boldsymbol{x})\,\mathrm{d}s, \\ &\nabla\cdot\boldsymbol{u} = 0, \\ &\boldsymbol{u}(\boldsymbol{\xi}(s,t)) = \int_{\boldsymbol{x}} \boldsymbol{u}(\boldsymbol{x})\delta(\boldsymbol{x}-\boldsymbol{\xi})\,\mathrm{d}\boldsymbol{x} = \boldsymbol{u_B}(\boldsymbol{\xi}(s,t)). \end{aligned} \tag{3.15}$$

This system of equations can be written as a Karush–Kuhn–Tucker (KKT) system of the from

$$\begin{bmatrix} A & Q \\ Q^\top & 0 \end{bmatrix} \begin{pmatrix} u^{n+1} \\ \lambda \end{pmatrix} = \begin{pmatrix} r_1 \\ r_2 \end{pmatrix} \tag{3.16}$$

with the following sub-matrices

$$Q \equiv [G, E^\top], \qquad \lambda \equiv \begin{pmatrix} p \\ \tilde{f} \end{pmatrix}, \qquad r_1 = r^n + bc_1, \qquad r_2 = \begin{pmatrix} -bc_2 \\ u_B^{n+1} \end{pmatrix}. \tag{3.17}$$

where the regularization (H) and interpolation (E) as well as the gradient (G) and the divergence (D) operator are chosen to be skewed-symmetric. $\tilde{f}$ is chosen such that $Hf = -E^\top \tilde{f}$. A LU-

decomposition of this system results in the projection method

$$\begin{aligned} Au^* &= r_1 \\ Q^\top B^N Q\lambda &= Q^\top q^* - r_2 \\ u^{n+1} &= u^* - B^N Q\lambda, \end{aligned} \tag{3.18}$$

where B^N is a N^{th} order approximation to A^{-1}. This system is relatively similar to the standard projection method, except for the pressure-projection step (step 2). The resulting matrix inversion required is not as straight-forward to solve, because the matrix $Q^\top B^N Q$ is an augmented matrix, where the augmented rows depend on the location of the interface. However, solving this augmented matrix is precisely what allows this method to correctly treat the pressure flux term, and results in the good results obtained (see later). Goza and Colonius (2017) successfully applied this method to the strongly-coupled FSI problem of an inverted 2D flag. This method is similar to the method of Lagrange multipliers used with finite-elements formulation to impose weak boundary condition on non-matching interface problems.

The boundary data immersion method (Maertens and Weymouth, 2015; Weymouth and Yue, 2011) is based on the analytical combination of the field equations of the two domain (solid and fluid) and the interfacial conditions into governing equations that are valid over the complete domain $\Omega_f \cup \Omega_b$. This analytical combination is achieve via a kernel interpolation that allows a field equation valid on the domain Ω_f to be extended into the complete domain Ω_ε

$$\mathcal{M}_\varepsilon(\boldsymbol{x},t) = \mathcal{F}_\varepsilon(\boldsymbol{x},t) + \mathcal{B}_\varepsilon(\boldsymbol{x},t), \tag{3.19}$$

where the extended fluid and body field equations are

$$\begin{aligned} \mathcal{F}_\varepsilon(\boldsymbol{x},t) &= \int_{\Omega_f} \mathcal{F}(\boldsymbol{x}_f,t)\mathcal{K}_\varepsilon(\boldsymbol{x},\boldsymbol{x}_f)\,\mathrm{d}\boldsymbol{x}_f, \\ \mathcal{B}_\varepsilon(\boldsymbol{x},t) &= \int_{\Omega_b} \mathcal{B}(\boldsymbol{x}_b,t)\mathcal{K}_\varepsilon(\boldsymbol{x},\boldsymbol{x}_b)\,\mathrm{d}\boldsymbol{x}_b. \end{aligned} \tag{3.20}$$

With the aim of removing the dependency of field equations on the variable of integration, a second order Taylor-series expansion results in the second-order BDIM equations

$$\boldsymbol{u}_\varepsilon = \mu_0^\varepsilon \boldsymbol{f} + (1-\mu_0^\varepsilon)\boldsymbol{b} + \mu_1^\varepsilon \frac{\partial}{\partial n}(\boldsymbol{f}-\boldsymbol{b}) \tag{3.21}$$

$$\boldsymbol{f} = \boldsymbol{u} + \boldsymbol{r}_{\Delta t}(\boldsymbol{u}) - \nabla p \tag{3.22}$$

where μ_0^ε and μ_1^ε are the zeroth and first moments of the kernel, respectively

$$\mu_n^\varepsilon = \int_{\Omega_f} (\boldsymbol{x}_f - \boldsymbol{x})^n \mathcal{K}_\varepsilon(\boldsymbol{x},\boldsymbol{x}_f)\,\mathrm{d}\boldsymbol{x}_f. \tag{3.23}$$

$\boldsymbol{f}$ are the fluid field equations (Navier-Stokes) and $\boldsymbol{b}$ is the body field equations. In the case of a

stationary body, those are simply $\boldsymbol{b} = 0$, however, they take a much more complex form in the case of fluid-structure interaction problems

$$\boldsymbol{b} = \frac{\partial \boldsymbol{\xi}}{\partial t}, \tag{3.24}$$

where $\boldsymbol{\xi}$ satisfies (2.4)-(2.6)-(2.7). This analytical combination of the field equation can be seen as a local averaging of the two sets of equations, both contributing in a region $\pm\varepsilon$ around the interface. For an incompressible viscous flow $\boldsymbol{r}_{\Delta t}(\boldsymbol{u})$ contains the convective and viscous terms. Second-order convergence was shown with respect to the kernel width ε. This convolution approach limits the applicability of the method to bodies with a non-zero thickness. Indeed, the convolution described in 3.20 is only valid over a domain of the same co-dimension as the final domain, and not for an interface. The minimum size of the body domain that is allowed is related to the compact support of the integration kernel $\mathcal{K}_\varepsilon$.

Used with a projection method, the intermediate velocity step is similar to a Direct forcing method (if we neglect the first moment terms), the difference comes from the pressure projection step

$$\nabla \cdot (\frac{\mu_0^\varepsilon}{\rho} \nabla p) = \nabla \cdot \boldsymbol{u}^*, \tag{3.25}$$

and the corrector step

$$\boldsymbol{u}^{n+1} = \boldsymbol{u}^* + \frac{\mu_0^\varepsilon \Delta t}{\rho} \nabla p. \tag{3.26}$$

Here the zeroth kernel moment acts as to prevent pressure flux across the immersed boundary. This treatment of the pressure flux ensures that the kinematic boundary condition is properly imposed on the pressure flux.

We note here that there are other ways to solve the *Navier-Stokes* equations, most notably, Chapman–Enskog theory links macroscopic variables (density ρ, momentum $\rho\boldsymbol{u}$, viscosity μ) to mesoscopic variables (distribution functions f, relaxation parameter τ). From this we can write the second-order flux tensor $\Pi_{\beta\gamma}$ as

$$\begin{aligned} \Pi_{\beta\gamma} &= \rho \boldsymbol{u}\boldsymbol{u} + p\boldsymbol{I} - \mu[\nabla \boldsymbol{u} + (\nabla \boldsymbol{u})^\top], \\ &= \sum_{\alpha=0}^{N} (\boldsymbol{e}_\alpha)_\beta (\boldsymbol{e}_\alpha)_\gamma \left[f_\alpha^{eq} + \left(1 - \frac{1}{2\tau}\right) f_\alpha^{neq} \right], \end{aligned} \tag{3.27}$$

where $\boldsymbol{e}_\alpha$ is the particle velocity in the α direction, and f_α^{eq} and f_α^{neq} are the (prescribed) equilibrium and non-equilibrium distribution functions, respectively. Because this flux tensor contains all the viscous and pressure terms, we do not need to solve for the pressure. The Hybrid Lattice-Boltzmann-Immersed-Boundary-method (Liu et al., 2020) allows to simply write the *Navier-Stokes* equations as

$$\frac{\partial \rho \boldsymbol{u}}{\partial t} + \nabla \cdot \Pi_{\beta\gamma} = \boldsymbol{f}. \tag{3.28}$$

Which automatically satisfies continuity. Here there is no need to solve an elliptic equation to get the pressure, but the forcing term that imposes the boundary conditions ($\boldsymbol{f}$) must be divergence free. This term can be efficiently obtain in the Lattice-Boltzmann framework from an adapted IBM kernel (F.-B. Tian et al., 2011; Xu et al., 2018).

While the focus of this section was on finite-volume and finite-difference methods, we not that other discretization of the *Navier-Stokes* equations have been successfully used with Cartesian grid methods. The finite element method (CD and DG alike) have long made used of non-body-conforming method to impose weak boundary conditions via the method of Lagrange multipliers (Glowinski et al., 1998) or Nitsche's method (Alauzet et al., 2016). Discontinuous Galerkin method (the finite-volume method can be seen as a special case of DG) is also well suited for cut-cell type approaches and other Cartesian grid methods.

To summarise the simple analysis if the existing methods and the current research path in Cartesian gird method, we have a wide range of methods that are available to impose boundary conditions on non-body conforming meshes. They mostly differ in the way an additional forcing is computed. However, because of the algorithm used the solve the coupled *Navier-Stokes* and continuity equations, those boundary conditions are sometimes only approximately imposed and with poor convergence properties (worst than second-order). We have seen that some methods correctly treat the pressure flux boundary condition during the pressure-projection step, and those methods are expected to perform significantly better than other ones. This essentially prevents the fluid from leaking across the boundary.

Other issues present in Cartesian gird method have not been discussed here. Perhaps the most important, at least for high Reynolds number flow, is the ability of the method to properly resolve the boundary layer and to correctly estimate the wall shear stresses. Efficient representation on the location of the immersed interface is also a complex task, level-set functions can be used, which also allow for a trivial evaluation of the normal distance, however, it is not clear how to extend those methods for an open interface. Load calculation in immersed boundary methods is also an area of active research (Goza and Colonius, 2017).

3.1 1D FSI Model

We know consider a canonical uni-dimensional fluid-structure interaction problem that contains all the desired physical and numerical complexities (large displacements, thin structure, small mass ratios) that are usually found in real-life fluid-structure interaction problems.

A piston is placed inside a circular pipe, the piston is assumed to be completely impermeable and has no friction with the side of the pipe. This piston is maintained in place with a spring with stiffness κ, see figure (3.1)

The position of the piston is initially set such that the spring is extended by an amount

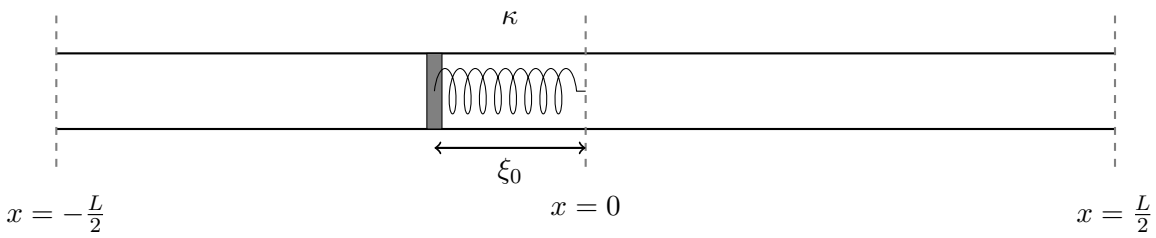

Figure 3.1: 1D FSI model schematic.

ξ_0. Once released, the spring will pull the piston back toward its attachment point. Because the problem is assumed to be periodic (any quantity ϕ satisfies $\phi(-L/2) = \phi(L/2)$), the piston accelerate the fluid contained in the pipe and we have a simple mass-spring oscillator system of the from

$$(m_p + m_f)\ddot{\xi} + \kappa\xi = 0, \tag{3.29}$$

where m_p is the mass of the piston and m_f is the mass of fluid contained in the pipe. The natural frequency of this simple system is

$$\omega = \sqrt{\frac{\kappa}{m_p + m_f}}. \tag{3.30}$$

The motion of the fluid inside the pipe is governed by the simplified uni-dimensional *Navier-Stokes*

$$\frac{\partial u}{\partial t} = -\frac{1}{\rho}\frac{\partial p}{\partial x}, \tag{3.31}$$

and continuity equations

$$\frac{\partial u}{\partial x} = 0. \tag{3.32}$$

After the release of the piston, the spring will accelerate the piston to a certain velocity, we know that the velocity of the fluid must immediately match that of the piston in order to satisfy continuity

$$u(t) = u_p. \tag{3.33}$$

Integrating (3.31) in time

$$u(t) - u_0 = -\int_0^t \frac{1}{\rho}\frac{\partial p}{\partial x}\,\mathrm{d}t. \tag{3.34}$$

Starting from an quiescent fluid, and substituting the solution, we find that the pressure gradient impulse must match the piston's velocity

$$u_p = -\int_0^t \frac{1}{\rho}\frac{\partial p}{\partial x}\,\mathrm{d}t. \tag{3.35}$$

For a Cartesian method to be successful in solving this uni-dimensional FSI problem, it must be able to generate the correct pressure gradient impulse in a single time-step. This physically trivial but numerically not trivial problem will allow us to compare different Cartesian grid methods and assess their ability to perform on much more complex FSI problems.

Cartesian Grid Discretization

Our aim is to rewrite system (3.33)-(3.34) into single equation of the form

$$u_\epsilon = g(u,p) + h(V), \tag{3.36}$$

that can efficiently be solved on a Cartesian grid. $g(\cdots)$ and $h(\cdots)$ are two functions that impose the boundary condition between the fluid and the solid implicitly. We will use an idea similar to that of BDIM, but we will not assume a particular kernel for now. Our two unknown function become

$$\begin{aligned} g(u,p) &= \int_\Omega \left(u - \int_0^t \frac{\partial p}{\partial x}\,dt\right) K_\epsilon(x,x_f)\,\mathrm{d}x_f = \mu_f\left(u - \int_0^t \frac{1}{\rho}\frac{\partial p}{\partial x}\,dt\right), \\ h(V) &= \int_\Omega V K_\epsilon(x,x_d)\,dx_d = \mu_b V, \end{aligned} \tag{3.37}$$

where the exact form of both kernel that are used to blend the solid a fluid equation together is unknown. However, your simple 1D case allows us to show that both μ_f and μ_b are linked. Taking the divergence of equation (3.36) for a stationary fluid $u = 0$ and requiring that $\partial_x u_\epsilon = 0$ gives

$$\frac{\partial}{\partial x}\left(\mu_f \frac{\Delta t}{\rho}\frac{\partial p}{\partial x}\right) = \frac{\partial}{\partial x}\left(\mu_b V\right). \tag{3.38}$$

We know that the interface will generate a constant pressure gradient whose jump across the interface is proportional to the acceleration of the interface

$$[\![p]\!]_\Gamma = -L\frac{\partial p}{\partial x} = \rho L \frac{V}{\Delta t} \tag{3.39}$$

where ρL is he mass of fluid in the domain. This can be used to simplify the previous expression

$$-\frac{\partial}{\partial x}\mu_f = \frac{\partial}{\partial x}\mu_b, \tag{3.40}$$

from which we deduce

$$\mu_b = 1 - \mu_f. \tag{3.41}$$

The exact form of the kernel μ_f is still unknown, but we know have a relationship between the kernel for the fluid and the body.

Extending BDIM for thin bodies

One way of extending the BDIM to thinner bodies, while keeping the co-domain dimensions the same, is to adjust the support of the kernel. For the method to be effective, at least on grid point must be fully inside the body (this means that $\mu_0^\varepsilon = 0$ somewhere). This ensures that the correct boundary conditions (for velocity and pressure) are correctly imposed on at least a grid point. On way to achieve this is to reduce the compact support of the kernel directly. This allows the

Table 3.1: Results for the 1D FSI Piston case.

Cartesian Method	$\max(\lvert u - V \rvert)$
IBM	9.375×10^{-1}
Direct Forcing	9.375×10^{-1}
BDIM	1.777×10^{-10}
BDIM new kernel	3.306×10^{-10}
IIM	2.006×10^{-9}
IBPM	1.483×10^{-11}
cIBM	9.717×10^{-1}

thickness of the body to be reduced. For a general n-dimensional body, the maximum distance two grid points can be apart is $\sqrt{n}$. By generating a body with a thickness of $\sqrt{n}+1$ and changing the support of the kernel to $\varepsilon = 0.5$, we ensure that in any given body configuration, at least 1 grid point is fully inside the body and thus the correct boundary conditions are imposed. We can then use the relationship derived earlier (equation 3.41) to link the fluid and body kernels. As will be shown in the next section, this allows to model bodies much thinner than the standard BDIM kernel.

Results

This section presents results for the uni-dimensional piston case. The domain is discretized using 32 grid points, we found that the solution is independent in the spacial discretization. Because no convective nor diffusive process are involve there is no time-step restriction. We perform a single iteration using the algorithm described earlier and we compared the velocity field obtained to the analytical solution. A staggered arrangement of the variables is used. The interface is placed randomly at the center of this domain. Second-order central difference schemes are used for all the numerical operators. Convergence for the Jacobi solver are set to a reduction of the initial residuals by 10 order. Results are presented in table 3.1[2].

Of the six methods used to solve the 1D piston problem, only three recover the correct solution. The standard IBM and the Direct Forcing methods poorly enforce the boundary condition on the final velocity field. The immersed interface method is also unable to solve this problem; however, as we know the solution we can use it to solve the problem by prescribing the pressure jump $[\![p]\!] = \rho L/\Delta t$. When part of a Peskin-type forcing are used with the IIM results are only slightly better than the IBM.

The immersed boundary projection method recovers the correct velocity field with a single step of the fractional step algorithm by solving the augmented matrix system. In this case, the

[2]Notebook containing the algorithms and the solutions can be found at: `https://github.com/marinlauber/FlexibleSheets/tree/master/1D-Piston`

matrix is augmented of only 1 row/column. We note however that twice as many Jacobi steps are required for convergence compared to BDIM.

The boundary data immersion method is also able to recover the exact solution. We will note that with this method the body is required to have a substantial thickness (4 cells in our case) in order to provide accurate results. This is related to the support of the kernel used to convolve the two domains. The modified BDIM kernel allows to have a much thinner body, and recover the exact results. This simple example exposed some aspects of Cartesian grid method that are important to simulate thin, flexible bodies.

3.1.1 Circular Disk

To emphasise the importance of correctly treating the pressure flux term in Cartesian grid methods, we use an added mass problem described in Fernando et al. (2020). An initially stationary thin disk is accelerated, during the acceleration phase the flow is fully described by a potential model and the added mass force acting on this disk takes the trivial from

$$F_{AM} = C_a \rho D^3 a, \tag{3.42}$$

where C_a is the added mass coefficient for a circular disk

$$C_a = \frac{1}{3} = \left(\frac{F_{AM}}{\rho D^2 U^2}\right)\left(\frac{U^2}{aD}\right). \tag{3.43}$$

The last term is the non-dimensional acceleration $a^* \equiv aD/U^2$. The initial impulse given to the circular disk results in a potential flow. The resulting pressure force[3] should match the potential flow solution.

A resolution of 512 cells per diameters is used to ensure that the fine scales of the flow are properly captured (this resolution is based on the study of Fernando et al. (2020)). Because of the symmetry of the problem, we only model a quarter of the disk. A uniform grid region of $[1.25 \times 1.25 \times 1.25]$ disk radius is used to properly capture the vortex roll-up and the wake of the disk. Grid stretching is used to fill the rest of the domain until it reaches the total size of $[20 \times 6.66 \times 6.66]$ disk radius. The no-slip boundary condition is applied on the disk. Instead of accelerating the disk itself, we accelerate the fluid inside the domain. This ensures that the wake is always located in the Cartesian region of the grid. Inlet boundary conditions are prescribed as $\boldsymbol{u} = (U, 0, 0)$, where U is derived from the acceleration profile (an hyperbolic tangent in this case, see Fernando et al. (2020)). The natural convective exit is applied on the face of the domain downstream of the body. Two symmetric boundary conditions are used on the symmetry planes. All other boundaries use the no-penetration condition.

We compare two immersed boundary method, the boundary data immersion method (Maertens and Weymouth, 2015) and a Direct forcing method (Fadlun et al., 2000). The first method pro-

[3]We use an explicit discretization of the diffusive term, this means that the first time step is only composed of a pressure force and no viscous force.

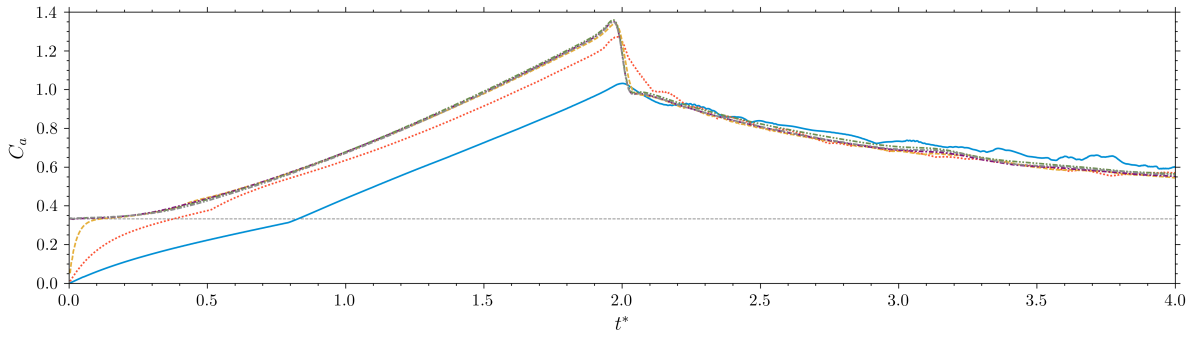

(a)

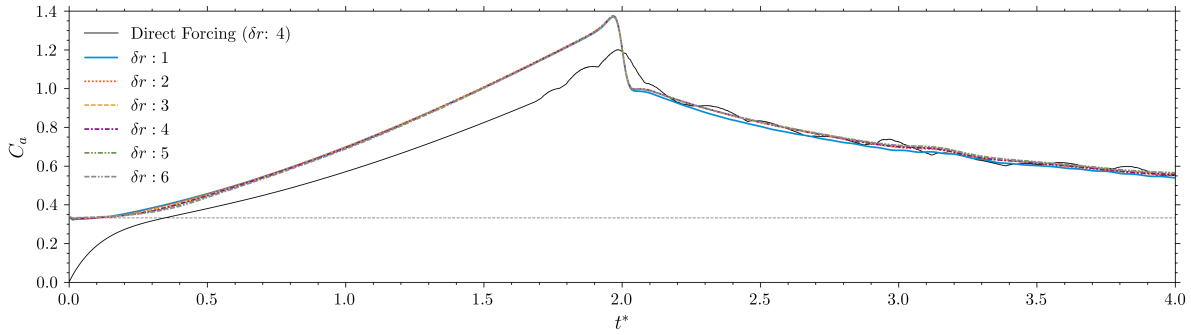

(b)

Figure 3.2: Added-mass coefficient against non-dimensional time $t^* = tU_1/D$ for the impulsively accelerated disk, acceleration modulus $a^* = 0.5$ and $Re = 1.25 \times 10^5$. Boundary data immersion method (a) with varying disk thickness (δr) and a modified BDIM kernel and a direct forcing method (b). The dashed gray line is the potential flow added-mass coefficient ($C_a = 1/3$).

vides the correct treatment of the pressure flux across the interface, while the second method only provides changes to the predictor step by imposing the kinematic boundary condition on the velocity field. This results in a poor imposition of the boundary condition on the final velocity field, see figure 3.3a where some flow through the disk can be observed.

Figure (3.2a) presents the results for the standard second-order BDIM. We observe a strong dependency on the disk thickness on the force measured during the initial acceleration phase ($t^* < 2$). To recover the correct added-mass force, the thickness of the disk cannot be less than $\delta r = 4$, this is related to the compact support of the kernel used to convolve both solid and fluid domain. Indeed, with a compact support of 2 the domain cannot be properly convoluted together if the thickness is less than twice the kernel support (best case scenario) and the pressure flux term is not properly switched of and fluid is allowed to leak trough the disk. The exact same behaviour is observed with the direct forcing method that simply does not impose the boundary conditions on the pressure fluxes during the projection step, see figure 3.2b.

In order to reduce the thickness of the body, the support of the kernel must be reduced as well. By keeping a ratio of disk thickness-to-kernel-support of 2, the convolution can be correctly performed and the correct boundary condition are impose on the pressure projection step. This allows the correct added-mass force to be obtained for much thinner disks, see figure 3.2b.

While the test case above would be trivially solved by a body fitted discretization of the fluid domain, it correctly captures the complexity of moving boundaries where pressure forces are the dominant driver of the fluid, for example a butterfly wing.

3.1.2 Ellipsoidal wing

Dynamically moving object with complex motion (coupled axial and rotational motion) are hard to simulate with body-fitted methods. Re-meshing is required at every time step, which penalizes the computational time. Cartesian grid methods, on the other hands, can deal with moving body problem with ease. We demonstrate this with an ellipsoidal wind example. This is an idealised fly wing. The geometry is defined as a ellipsoidal, following (Bos et al., 2013; Sane and Dickinson, 2001; Wang et al., 2004; Zheng et al., 2020)

$$\frac{x^2}{a^2} + \frac{y^2}{b^2} + \frac{z^2}{c^2} = 1, \tag{3.44}$$

where $a = 0.5$, $b = 0.05$ and $c = 1$. The motion is completely described by the three following Euler angles

$$\varphi(t) = A_\varphi \cos(2\pi f_r t) \tag{3.45}$$

$$\theta(t) = A_\theta \sin(2\pi f_\theta t) \tag{3.46}$$

$$\alpha(t) = \frac{\pi}{2} - A_\alpha \cos(2\pi f_r t + \xi) \tag{3.47}$$

A_i is the amplitude of the respective motion and f_r is the frequency of the stroke. For figure-of-O pattern $f_\theta = 2f_r$. (here we use $f_\theta = f_r = 0.5$, such that the stroke motion is confined into the

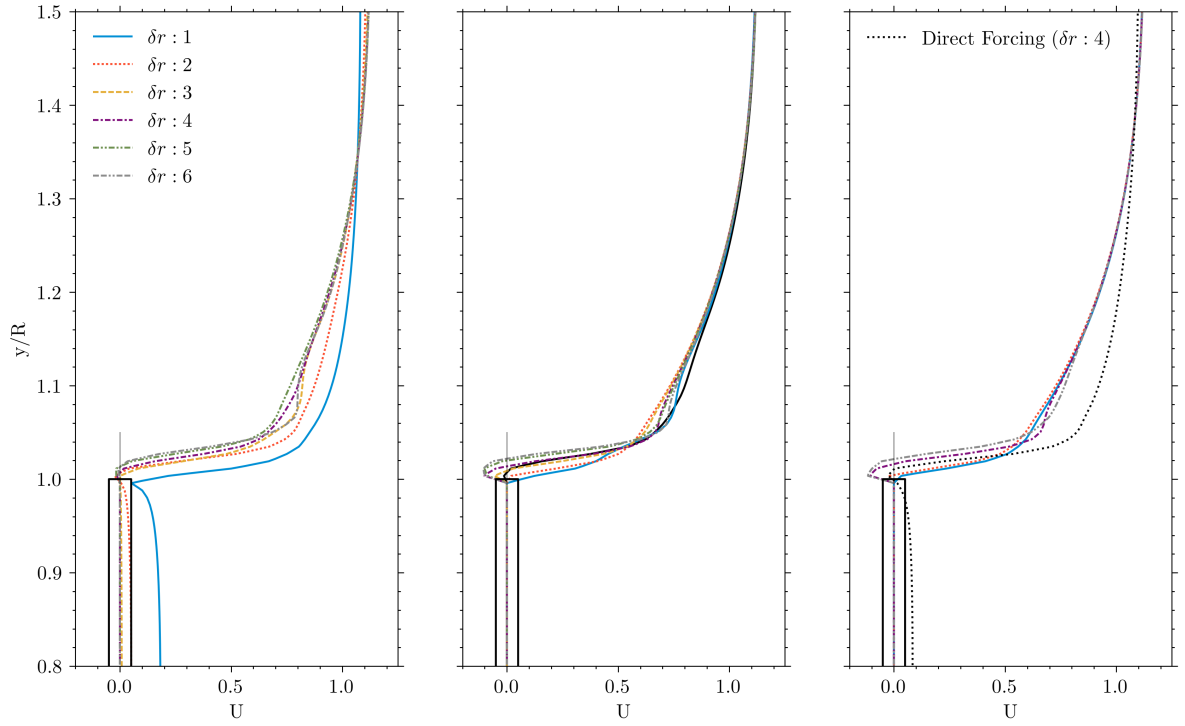

(a)

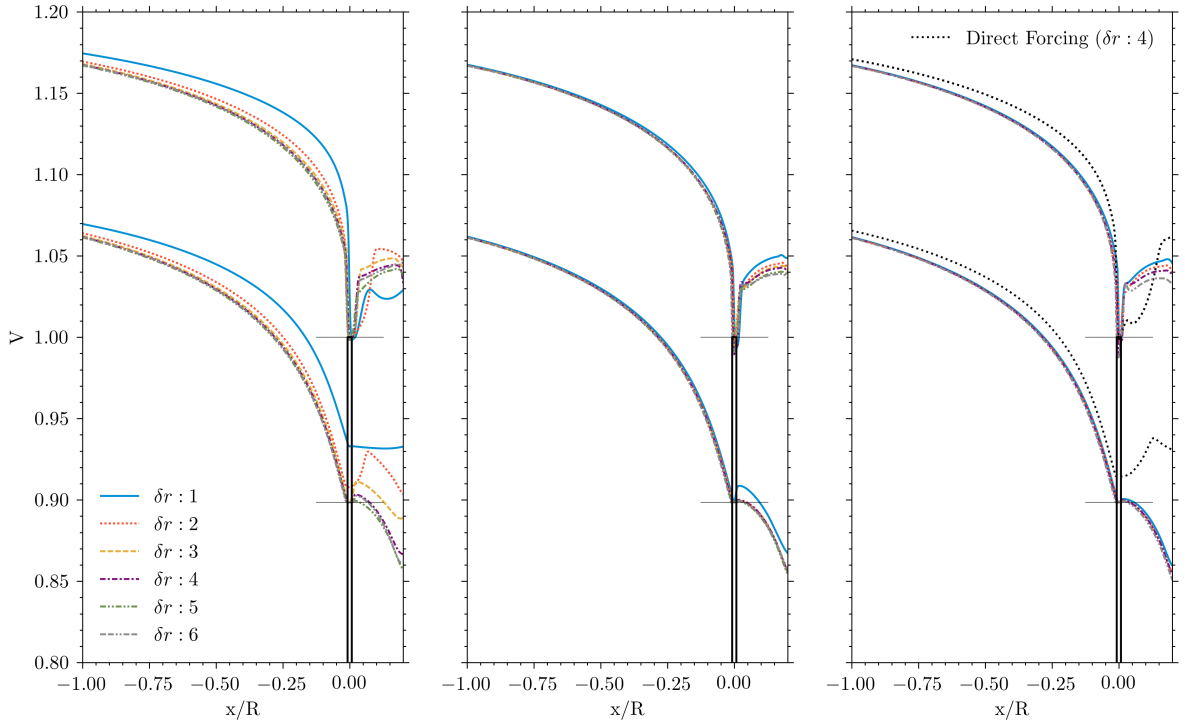

(b)

Figure 3.3: Horizontal (a) and vertical (b) velocity profiles close to the impulsively accelerated disk, acceleration modulus $a^* = 0.5$ and $Re = 1.25 \times 10^5$ for different disk thickness (δr). Left panels are for boundary data immersion method, middle panels are for the modified kernel and the right panels contain some of the modified kernel results superimposed with a Direct forcing result. (Thickness of the disk not to scale.)

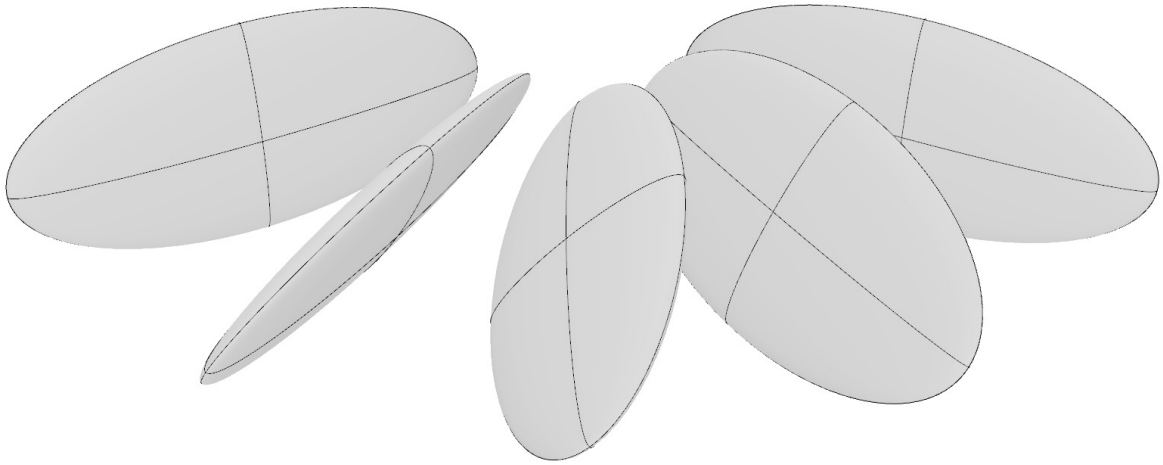

Figure 3.4: Ellipsoidal wing at different time during an oscillatory period ($t/T \in \{0., 1/8, 1/4, 3/8, 1/2\}$). Motion kinematics are: $f_\theta = f_r = 0.5$, $A_\varphi = 0.35\pi$ and $A_\alpha = \pi/4$.

$x-z$ plane.). ξ is the deviation of the angle of attack to the stroke (set to zero in the following). The stoke amplitude $A_\varphi = 0.35\pi$ and $A_\alpha = \pi/4$, see figure 3.4.

A resolution of 48 grid point along the chord of the wing is used, resulting in a thickness of less than 4 grid points. For this reason, we use a modified kernel ($\varepsilon = 0.5$) to represent the body. A Cartesian region of size $[3 \times 2 \times 2]$ chords centered around the center of rotation of the wing ensures that the wing is always properly discretized, regardless of the motion. Grid stretching is used to fill the rest of the domain. The final domain size is $[6 \times 6 \times 6]$ chords. The no-slip boundary condition is applied on the wing and the no-penetration is applied on all exterior boundaries of the computational domain. The wing evolves in a quiescent flow $\boldsymbol{u} = (0, 0, 0)$.

The force acting on the wing are described in terms of the lift and drag coefficients

$$C_L = \frac{F_y}{\frac{1}{2}\rho U_{ref}^2 S}, \qquad C_D = \frac{F_x \cos(\varphi) - F_z \sin(\varphi)}{\frac{1}{2}\rho U_{ref}^2 S} \tag{3.48}$$

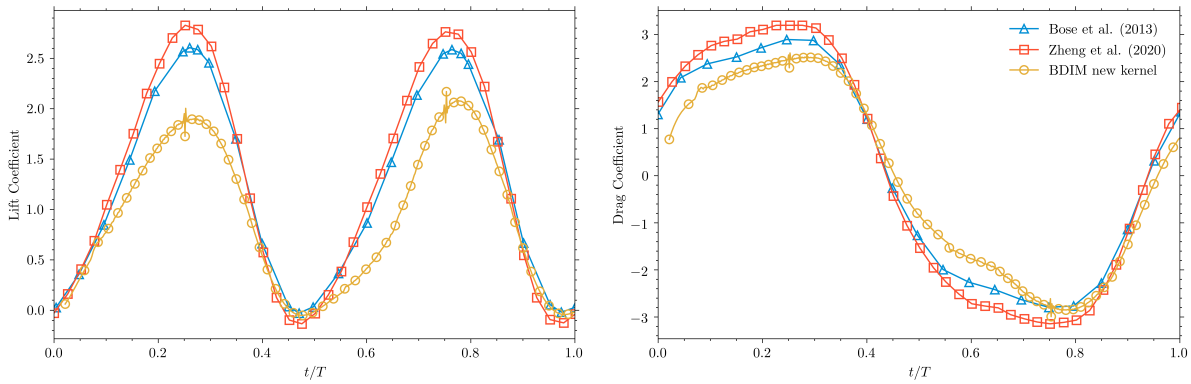

(a) (b)

Figure 3.5: Lift and drag coefficients for an oscillatory period. Motion kinematics are: $f_\theta = f_r = 0.5$, $A_\varphi = 0.35\pi$ and $A_\alpha = \pi/4$. Results for the new kernel are only preliminary.

where $S = \pi/2$ is the area of the ellipsoidal wing. The reference velocity is

$$U_{ref} = f_r \int_0^{1_r} \sqrt{\dot{\varphi}^2 + \dot{\theta}^2}\, \mathrm{d}t R_g \tag{3.49}$$

and the radius of gyration (R_g) is defined as

$$R_g = \sqrt{\frac{1}{S} \int_0^R cr^2\, \mathrm{d}r}. \tag{3.50}$$

Preliminary results are shown on figure 3.5. Those results are only preliminary since oscillations are observed at the peak of the lift. The cause of those oscillations is not entirely clear. Also the force magnitude is greatly underestimated compared to the two other studies.

3.1.3 Flat Plate at Angle-of-Attack at Low Reynolds Numbers

Taira and Colonius (2009) and Taira et al. (2007) presented a test case with a thin plate at an range of angle of attack for different Reynolds numbers (100 to 5000). This low Reynolds number flow is dominated by a strong shear layer that rolls-up on top of the plate. Depending on the Reynolds number this shear layer becomes unstable and this behaviour is reflected in the wake ($Re \gtrapprox 300$). This test case allows to compare the BDIM with the IBPM. Two methods that showed promising results for the one-dimensional test case.

We select the case of a plate at an angle of attack of 30 degrees and a Reynolds number of 300 the aspect ratio of the plate is set to 2. Force history and instantaneous flow structures are available for this case to compare both methods. A resolution of 64 grid point along the chord is selected for the uniform grid region. The domain extends 6 chords upstream and 12 chords downstream of the plate. The size of the test section is set to 10×10 chords. The uniform section is $[5 \times 2 \times 3]$ chords and is centered around the body. Grid stretching is used to fill the rest of

the domain. The symmetry of the problem (for this low Re case) is used to model only half the span of he plate. Symmetric boundary conditions are imposed on this center plane. The flow velocity is prescribed at the inlet $\boldsymbol{u} = (1, 0, 0)$, while a natural convective boundary condition is used for the outlet. The no-slip boundary condition is applied on the plate. The no-penetration is enforced on all other boundaries.

Time-averaged (after a long time) forces are analysed in terms of lift and drag coefficients, defined as

$$C_L = \frac{F_y}{\frac{1}{2}\rho U_\infty^2 A}, \qquad C_D = \frac{F_x}{\frac{1}{2}\rho U_\infty^2 A}, \tag{3.51}$$

where ρ and U_∞ are the free-stream density and velocity, respectively. Results are presented on figure 3.7. An excellent agreement is found with the average lift coefficient (see figure 3.7a) with an error of $\sim 3\%$. The drag coefficient is greatly overestimated compared to the IBPM method. While the lift is mostly due to pressure forces (90% of the total force), the drag is made of 60% pressure and 40% viscous forces. This makes the numerical integration of the wall shear stress on the body extremely important. This is hard in immersed boundary methods, especially when a strong shear layer or boundary layer develops because the wall shear stresses are interpolated using values away from the wall

$$\boldsymbol{F}_f = \nu \int_\Omega \boldsymbol{n} \cdot [\nabla \boldsymbol{u} + (\nabla \boldsymbol{u})^\top] \delta_\varepsilon^+ \, \mathrm{d}\boldsymbol{x}, \tag{3.52}$$

where δ_ε^+ is a kernel centered ε away from the body. This is a known issue in IBM in general (Pourquie, 2008). This also emphasise the importance of a good pressure treatment at the interface to get proper lift characteristics. The lift obtained on the plate is mostly due to the circulation of the vortex generated by the plate. While the initial wake is identical to that of Taira and Colonius (2009), we note that the final wake is much more messy than our, which would also explain the differences in the drag, see 3.6. These horse-shoe-like structures present on the center of the plate are not seen in the experiments form Freymuth et al. (1987), although they are a a much higher Reynolds-number. To make sure that the differences in the wake is not due to the symmetric boundary condition forcing the flow over the plate to be symmetric, we ran a case with the complete span, but the results were identical.

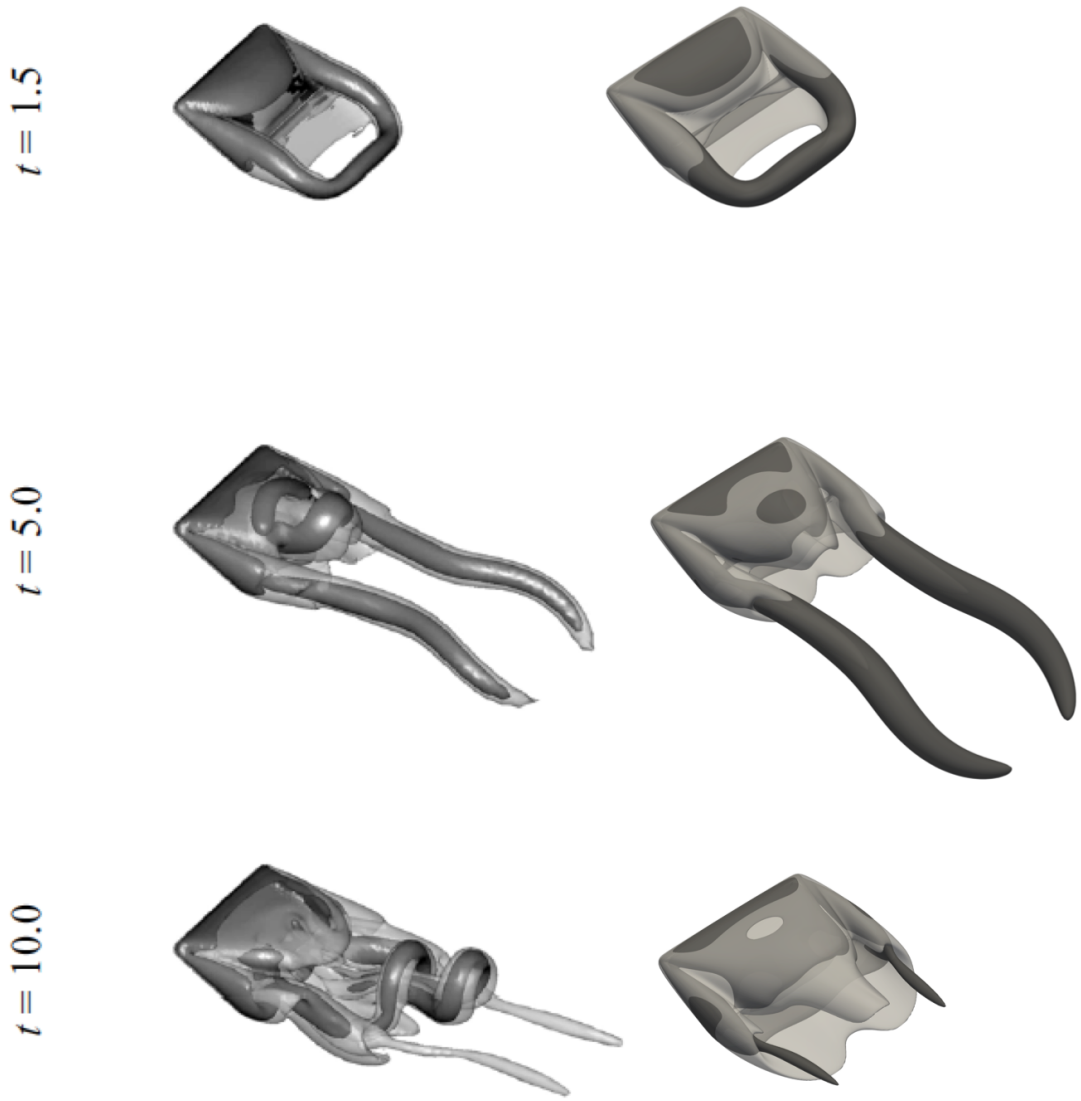

Figure 3.6: Vortical structure in the wake the flat plate of $AR = 2$ at $\alpha = 30^\circ$ and $Re = 300$ at time $t = 1.5$. Shown are the iso-surface of $\|\omega\|_2 = 3$ in light grey with vortex cores highlighted by the iso-surface of $\mathcal{Q} = 3$ in dark grey.

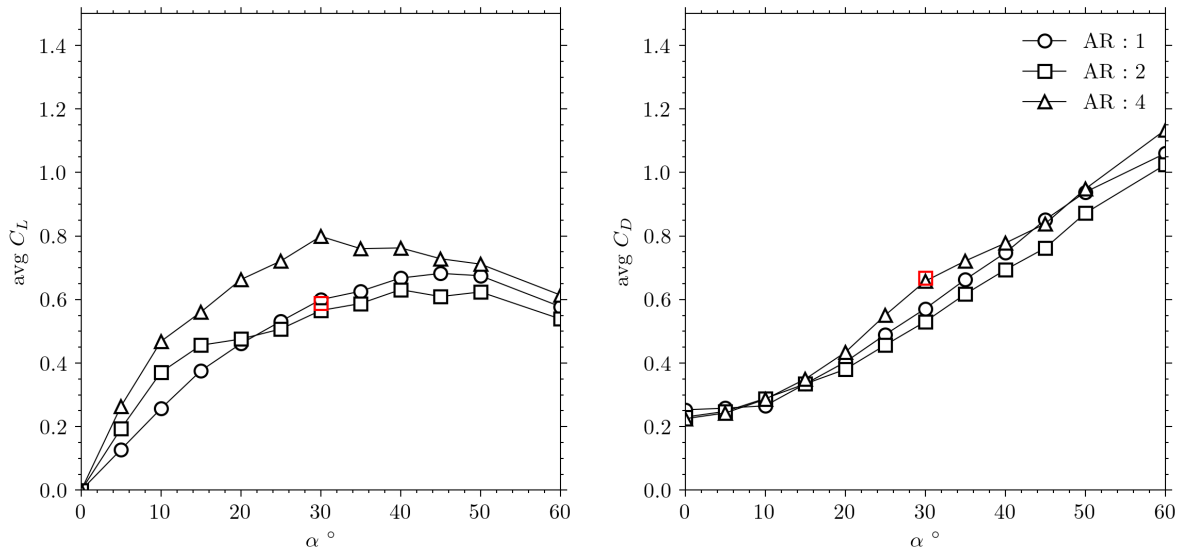

(a) (b)

Figure 3.7: Average lift (a) and drag (b) coefficient for the flat plate at $\alpha = 30°$ and $Re = 300$ for different aspect ratio from Taira and Colonius (2009). BDIM results (red squares) are for $\alpha = 30°$, $AR = 2$.

4 Future Work and Conclusion

While the focus has been mostly on the Cartesian grid side of the project, there are some aspects of the rest of the project that deserve discussion. First, the structural modelling of thin shells/membranes, and perhaps more importantly the coupling of this structural model and the fluid through the boundary conditions described in section 2.

All the thin structures described in the preceding section have the same characterises; their thickness is usually negligible, their bending stiffness is negligible compared to their membrane stiffness and they can accommodate different types of nonlinearities (material and geometrical). These are usually described using Kirchhoff-Love or Reissner-Mindlin theories. Hyper-elasticity is also extensively used to model materials characterised by nonlinearities. A wide variety of model are used to model this type of structures in fluid-structure-interaction applications.

4.1 Modeling Thin Shells/Membranes

Lagrange function space are usually used within the finite-element framework to discretize the equations of motion, recently isogeometric analysis is gaining some considerable attention due to its ability to efficiently link CAD to analysis. In addition the use of NURBS-based function space allow high continuity to be obtained efficiently.

Thin-shell structures are defined as extremely thin structures with very high membrane stiffness, but almost no bending stiffness. The Kirchhoff-Love shell theory is particularly well suited to describe the kinematic of thin structures where is not necessary to consider the out-of-plane deformation (L. Chen et al., 2014; Karagiozis et al., 2011). This means that the angle of rotation (ψ) is a function of the vertical displacement (w) field

$$\psi_x = \frac{\partial w}{\partial x} = w_{,x}, \qquad \psi_y = \frac{\partial w}{\partial y} = w_{,y}. \tag{4.1}$$

This makes the vertical displacement field the only variable. When the slenderness of the structure is very large, the Kirchhoff-Love shell theory can be augmented with the hypothesis of negligible bending stiffness, collapsing the equations to that of a membrane.[1]

Although much smaller than the membrane stiffness, the bending stiffness of thin-shell plays a crucial role in the wrinkling patterns that forms on the shell. From a computational point of view, inclusion of a small bending stiffness will allow those wrinkles to be modelled, but the size of the elements has to be chosen such that they are smaller than the wrinkling wavelength. This can be a serious problem for large scale membranes structures. It is not uncommon to have finite element sizes that do not allow capturing these fine-scale deformations. When wrinkling cannot

[1] Membranes are structures with negligible bending stiffness, thin shell have some bending integrity and plates cannot neglect the out-of-plane deformations, those are better described by the Mindlin–Reissner plate theory.

be resolved, Tension-Field (TF) theory (Wagner and Flugtechn, 1929) can be used to account for the wrinkling pattern, however this method doesn't allow to precisely determine the wrinkling pattern that develop, only the stress distribution associated with a wrinkling direction.

In addition to responding by membrane and bending actions, plates/shells incorporate coupling between the bending in x and y, a behaviour that beam elements cannot incorporate. This is the result of the presence of off-diagonal terms in the in the flexural rigidity matrix of Mindlin–Reissner plate theory (under plane stress assumption)

$$\begin{Bmatrix} M_x \\ M_x \\ M_{xy} \\ Q_x \\ Q_y \end{Bmatrix} = - \begin{bmatrix} D & \nu D & 0 & 0 & 0 \\ \nu D & D & 0 & 0 & 0 \\ 0 & 0 & \frac{1-\nu}{2} D & 0 & 0 \\ 0 & 0 & 0 & kGt & 0 \\ 0 & 0 & 0 & 0 & kGt \end{bmatrix} \begin{Bmatrix} \psi_{x,x} \\ \psi_{y,y} \\ \psi_{x,y} + \psi_{y,x} \\ \psi_x - w_{,x} \\ \psi_y - w_{,y} \end{Bmatrix},$$

where $D = Et^3/12(1-\nu^2)$ the fexural rigidity of the plate. The blue sub-set of the matrix is the Kirchhof-Love shell matrix. Studies conducted for thin structures employ more frequenlty Kirchoof-Love shell theory, see amongst others Bletzinger et al. (2018), Cirak and Radovitzky (2005), and Karagiozis et al. (2011) than the full Middlin-Reissner plate theory (Spenke et al., 2020).

4.1.1 Numerical solution for shell/membranes

Large deformation problem involving (potentially) wrinkled membranes require careful numerical treatment due to the singularity of the tangent stiffness matrix required to perform *Newton-Raphson* iterations. This matrix can become singular when the initial state of the membrane is undeformed (Nakashino et al., 2020). To obtain solution to steady-state membrane problem dynamic relaxation is used to provide initial conditions to the *Newton-Raphson* method. The idea behind dynamic relaxation is to obtain solution the steady-state problem by solving a pseudo-dynamic equivalent problem. Artificial damping force are added to the equations of motion to reach a steady-state solution from the pseudo-dynamic problem

$$\boldsymbol{M}\ddot{\boldsymbol{\xi}} = \boldsymbol{f}^{\text{ext}} - \boldsymbol{f}^{\text{int}} - \boldsymbol{f}^{\text{damping}}, \tag{4.2}$$

with $\boldsymbol{f}^{\text{damping}} = \mu \boldsymbol{M}\dot{\boldsymbol{\xi}}$ being an usual candidate (a damping term).

There are numerous (open source) framework that use the finite-element method to solve problems described by partial-differential equations, amongst the most common are *FEniCS, DEAL II., MOOSE, FEMPAR*. The aim is to use one of those framework to couple the in house code *Lotus* to obtain solution to the FSI problem of thin flexible sheets, which is the final aim of this thesis.

4.1.2 FSI Coupling

As detailed in the introduction, both systems are coupled through the boundary conditions. Accurate boundary conditions are required to properly solve the FSI problem, and as demonstrated in the uni-dimensional piston problem, not all immersed boundary method provide satisfactory results. In addition, the added-mass effect is know to be a severe limitation to partitioned algorithms (Causin et al., 2005) when light-weight structures are considered.

Additionally, computing loads on immersed interface was show not to be trivial, this will be especially important in the case of a plate/membrane that has close to zero thickness.

4.2 Conclusion

This report focused mostly on the Cartesian grid part of this project. With a detailed literature review of the different methods used in this field and using some benchmark test case we were able to define some critical points for those methods to be successful in a fluid-structure interaction context.

First, while imposing the correct boundary condition on the velocity field is important, imposing the boundary condition on the pressure is perhaps more important. We have seen that for our examples, where the pressure is what drives the flow, Cartesian grid method that do not treat the pressure correctly fail to provide satisfactory results. The uni-dimensional test case being an excellent example. Unsurprisingly, methods who failed on this simple test case, also failed on more complex cases where correctly resolving the pressure is important (accelerated disk).

Both the immersed boundary projection method and the boundary data immersion method correctly impose the boundary conditions on the velocity and pressure fields, however, further extension of the BDIM to thinner bodies (say zero thinckness) seems unrealistic, or at least not without changing a lot of the method. Indeed, the whole convolution idea would break-down a soon as the body has a dimension less than the fluid. While providing an exciting alternative, the IBPM requires solution to an augmented matrix that is not trivial to solve. This is believed to add significant computational complexity to the solution of the *Navier-Stokes* equations.

The second observation is of computational time, while a cut cell method might be best in terms of accuracy, the complex algorithm required to compute face information loses part of the attractive features of Cartesian grid methods.

The different test case used provide a wide range of challenges, from correctly resolving pressure forces to recover the correct added-mass to correctly resolving shear layer-drive flows. We observed some force oscillations on the dynamic ellipsoidal wing test case. The cause of those oscillations is still unknown, and further investigation are required. The main issue with noisy

forces is the instabilities that they will create in the structural solver.

While we focused mostly on the Cartesian grid side of this thesis, we do not forget that there are some other remaining challenges to be addressed. Depending of the applications, the wrinkling pattern that form on immersed plates/shells can play a crucial role in the fluid flow around the body (for example on a kite), and we have seen that these fine-scale structures can be expansive to resolve. In addition, the added-mass effect will add significant complication to the solution of the coupled system, especially considering that most of the application targeted are at low mass ratios.

References

Alauzet, Frédéric, Fabrèges, Benoit, Fernández, Miguel A., and Landajuela, Mikel (2016). "Nitsche-XFEM for the coupling of an incompressible fluid with immersed thin-walled structures". In: *Computer Methods in Applied Mechanics and Engineering* 301, pp. 300–335.

Bale, Rahul, Patankar, Neelesh A., Jansson, Niclas, Onishi, Keiji, and Tsubokura, Makoto (2020). "Stencil Penalty approach based constraint immersed boundary method". In: *Computers & Fluids*, p. 104457.

Bao, Yuanxun, Donev, Aleksandar, Griffith, Boyce E., McQueen, David M., and Peskin, Charles S. (2017). "An Immersed Boundary method with divergence-free velocity interpolation and force spreading". In: *Journal of Computational Physics* 347, pp. 183–206.

Bazilevs, Yuri, Takizawa, Kenji, and Tezduyar, Tayfun E (2013). *Computational fluid-structure interaction: methods and applications*. John Wiley & Sons.

Bletzinger, K.U., Wood, J.N., Breuer, M., De Nayer, G., Apostolatos, A., and Wüchner, R. (2018). "Numerical studies on the instantaneous fluid–structure interaction of an air-inflated flexible membrane in turbulent flow". In: *Journal of Fluids and Structures* 82, pp. 577–609.

Bos, Frank M., Oudheusden, Bas W. van, and Bijl, Hester (2013). "Wing performance and 3-D vortical structure formation in flapping flight". In: *Journal of Fluids and Structures* 42, pp. 130–151.

Causin, P., Gerbeau, Jean-Frédéric, and Nobile, Fabio (2005). "Added-mass effect in the design of partitioned algorithms for fluid-structure problems". In: *Computer Methods in Applied Mechanics and Engineering* 194, pp. 4506–4527.

Chen, Lei, Nguyen-Thanh, Nhon, Nguyen-Xuan, Hung, Rabczuk, Timon, Bordas, Stéphane Pierre Alain, and Limbert, Georges (2014). "Explicit finite deformation analysis of isogeometric membranes". In: *Computer Methods in Applied Mechanics and Engineering* 277, pp. 104–130.

Chen, Ye and Luo, Haoxiang (2018). "A computational study of the three-dimensional fluid–structure interaction of aortic valve". In: *Journal of Fluids and Structures* 80, pp. 332–349. ISSN: 10958622.

Chi, Cheng, Abdelsamie, Abouelmagd, and Thévenin, Dominique (2020). "A directional ghost-cell immersed boundary method for incompressible flows". In: *Journal of Computational Physics* 404, p. 109122.

Cirak, Fehmi and Radovitzky, Raúl (2005). "A Lagrangian-Eulerian shell-fluid coupling algorithm based on level sets". In: *Computational Fluid and Solid Mechanics 2003* 83, pp. 491–498.

Colonius, Tim and Taira, Kunihiko (2008). "A fast immersed boundary method using a nullspace approach and multi-domain far-field boundary conditions". In: *Computer Methods in Applied Mechanics and Engineering* 197.25-28, pp. 2131–2146.

de Langre, Emmanuel, Amandolese, Xavier, and Doare, Olivier (2016). *Fundamentals of Fluid-Solid Interactions [MOOC]*. Coursea.

Fadlun, E. A., Verzicco, R., Orlandi, P., and Mohd-Yusof, J. (2000). "Combined Immersed-Boundary Finite-Difference Methods for Three-Dimensional Complex Flow Simulations". In: *Journal of Computational Physics* 161.1, pp. 35–60.

Fedkiw, Ronald P., Aslam, Tariq, Merriman, Barry, and Osher, Stanley (1999). "A Non-oscillatory Eulerian Approach to Interfaces in Multimaterial Flows (the Ghost Fluid Method)". In: *Journal of Computational Physics* 152.2, pp. 457–492.

Fernando, J. N., Weymouth, Gabriel D., and Rival, D. E. (2020). "On the limits of added-mass theory in separated flows and with varying initial conditions". In: *Journal of Fluids and Structures* 93, p. 102835.

Freymuth, P., Finaish, F., and Bank, W. (1987). "Further visualization of combined wing tip and starting vortex systems". In: *AIAA Journal* 25.9, pp. 1153–1159.

Ghias, R., Mittal, R., and Dong, H. (2007). "A sharp interface immersed boundary method for compressible viscous flows". In: *Journal of Computational Physics* 225.1, pp. 528–553.

Gilmanov, Anvar, Le, Trung Bao, and Sotiropoulos, Fotis (2015). "A numerical approach for simulating fluid structure interaction of flexible thin shells undergoing arbitrarily large deformations in complex domains". In: *Journal of Computational Physics* 300, pp. 814–843.

Glowinski, R., Pan, T. W., and Périaux, J. (1998). "Distributed Lagrange multiplier methods for incompressible viscous flow around moving rigid bodies". In: *Computer Methods in Applied Mechanics and Engineering* 151.1-2, pp. 181–194.

Goldstein, D, Handler, R, and Sirovich, L (1993). "Modeling a No-Slip Flow Boundary with an External Force Field". In: *Journal of Computational Physics* 105, pp. 354–366.

Goza, Andres and Colonius, Tim (2017). "A strongly-coupled immersed-boundary formulation for thin elastic structures". In: *Journal of Computational Physics* 336, pp. 401–411.

Huang, Wei Xi and Tian, Fang Bao (2019). "Recent trends and progresses in the immersed boundary method". In: *Proceedings of the Institution of Mechanical Engineers, Part C: Journal of Mechanical Engineering Science* 233, pp. 7617–7636.

Jause-Labert, C., Godeferd, F. S., and Favier, B. (2012). "Numerical validation of the volume penalization method in three-dimensional pseudo-spectral simulations". In: *Computers and Fluids* 67, pp. 41–56.

Karagiozis, K., Kamakoti, R., Cirak, F., and Pantano, C. (2011). "A computational study of supersonic disk-gap-band parachutes using Large-Eddy Simulation coupled to a structural membrane". In: *Journal of Fluids and Structures* 27.2, pp. 175–192.

Kim, Woojin and Choi, Haecheon (2019). "Immersed boundary methods for fluid-structure interaction: A review". In: *International Journal of Heat and Fluid Flow* 75.July 2018, pp. 301–309.

Kolahdouz, Ebrahim M., Bhalla, Amneet P. S., Craven, Brent A., and Griffith, Boyce E. (2020). "An Immersed Lagrangian-Eulerian Method for Fluid-Structure Interaction". In: *arXiv preprint arXiv:2003.12046*, pp. 1–35.

Lai, Ming Chih and Peskin, Charles S. (2000). "An immersed boundary method with formal second-order accuracy and reduced numerical viscosity". In: *Journal of Computational Physics* 160.2, pp. 705–719.

Lee, Long and LeVeque, Randall J. (2003). "An Immersed Interface Method for Incompressible Navier–Stokes Equations". In: *SIAM Journal on Scientific Computing* 25.3, pp. 832–856.

LeVeque, Randall J. and Li, Zhilin (1994). "Immersed interface method for elliptic equations with discontinuous coefficients and singular sources". In: *SIAM Journal on Numerical Analysis* 31.4, pp. 1019–1044.

Liu, Fan, Liu, Gang, and Shu, Chang (2020). "Fluid–structure interaction simulation based on immersed boundary-lattice Boltzmann flux solver and absolute nodal coordinate formula". In: *Physics of Fluids* 32.4, p. 047109.

Lombardi, Matteo, Cremonesi, Massimiliano, Giampieri, Andrea, Parolini, Nicola, and Quarteroni, Alfio (2012). "A strongly coupled fluid-structure interaction model for wind-sail simulation". In: *4th High Performance Yacht Design Conference 2012, HPYD 2012*, pp. 212–221.

Luo, Yang, Xiao, Qing, Shi, Guangyu, Wen, Li, Chen, Daoyi, and Pan, Guang (2020). "A fluid–structure interaction solver for the study on a passively deformed fish fin with non-uniformly distributed stiffness". In: *Journal of Fluids and Structures* 92, pp. 1–44.

Maertens, Audrey P. and Weymouth, Gabriel D. (2015). "Accurate Cartesian-grid simulations of near-body flows at intermediate Reynolds numbers". In: *Computer Methods in Applied Mechanics and Engineering* 283, pp. 106–129.

McQueen, David M., Peskin, Charles S., and Zhu, Luoding (2007). "The Immersed Boundary Method for incompressible fluid-structure interaction". In: *Computational Fluid and Solid Mechanics* 1.212, pp. 26–30.

Mittal, Rajat and Iaccarino, Gianluca (2005). "Immersed Boundary Methods". In: *Annual Review of Fluid Mechanics* 37.1, pp. 239–261.

Nakashino, Kyoichi, Nordmark, Arne, and Eriksson, Anders (2020). "Geometrically nonlinear isogeometric analysis of a partly wrinkled membrane structure". In: *Computers and Structures* 239, p. 106302.

Peskin, Charles S (1972). "Flow patterns around heart valves: a numerical method". In: *Journal of computational physics* 10.2, pp. 252–271.

Peskin, Charles S. and Feller Printz, Beth (1993). "Improved Volume Conservation in the Computation of Flows with Immersed Elastic Boundaries". In: *Journal of Computational Physics* 105, pp. 33–46.

Platon, Jonathan (2011). "Computational fluid dynamics and fluid structure interaction of yacht sails". PhD thesis. The University of Nottingham.

Pourquie, M. (2008). "Accuracy close to the wall of immersed boundary methods". In: *IFMBE Proceedings* 22, pp. 1939–1942.

Ramolini, Anna (2019). "Implementation of a Fluid-Structure Interaction Solver for a Spinnaker Sail". In: *Journal of Sailing Technology* 4.1, pp. 1–16.

Renzsch, H. F. and Graf, K. U. (2014). "Fluid Structure Interaction Simulation of Spinnakers – Getting Closer to Reality". In: *International Journal of Small Craft Technology* 156.B2, pp. 71–80.

Richter, H.J., Horrigan, K.C., and Braun, J.B. (2003). "Computational Fluid Dynamics for Downwind Sails". In: *proceedings of the 16th Chesapeake Sailing Yacht Symposium.*

Sane, S. P. and Dickinson, M. H. (2001). "The control of flight force by a flapping wing: Lift and drag production". In: *Journal of Expiremental Biology* 204.19, pp. 2607–2626.

Spenke, Thomas, Hosters, Norbert, and Behr, Marek (2020). "A multi-vector interface quasi-Newton method with linear complexity for partitioned fluid–structure interaction". In: *Computer Methods in Applied Mechanics and Engineering* 361, p. 112810.

Taira, Kunihiko and Colonius, Tim (2009). "Three-dimensional flows around low-aspect-ratio flat-plate wings at low Reynolds numbers". In: *Journal of Fluid Mechanics* 623, pp. 187–207.

Taira, Kunihiko, Dickson, William B., Colonius, Tim, Dickinson, Michael H., and Rowley, Clarence W. (2007). "Unsteadiness in flow over a flat plate at angle-of-attack at low reynolds numbers". In: *Collection of Technical Papers - 45th AIAA Aerospace Sciences Meeting* 13.January, pp. 8791–8806.

Tian, Fang-Bao, Luo, Haoxiang, Zhu, Luoding, Liao, James C., and Lu, Xi-Yun (2011). "An efficient immersed boundary-lattice Boltzmann method for the hydrodynamic interaction of elastic filaments". In: *Journal of Computational Physics* 230, pp. 7266–7283.

Trimarchi, D., Turnock, S. R., Taunton, D. J., and Chapelle, D. (2010). "The use of shell elements to capture sail wrinkles, and their influence on aerodynamic loads". In: *RINA - International Conference - Innovation in High Performance Sailing Yachts, Papers*, pp. 33–45.

Tullio, M. D. de and Pascazio, G. (2016). "A moving-least-squares immersed boundary method for simulating the fluid–structure interaction of elastic bodies with arbitrary thickness". In: *Journal of Computational Physics* 325, pp. 201–225.

Vanna, Francesco De, Picano, Francesco, and Benini, Ernesto (2020). "A sharp-interface immersed boundary method for moving objects in compressible viscous flows". In: *Computers and Fluids* 201, p. 104415.

Wagner, H and Flugtechn, Z (1929). *Motorluftschiffahrt 20.*

Wang, Z. Jane, Birch, James M., and Dickinson, Michael H. (2004). "Unsteady forces and flows in low Reynolds number hovering flight: Two-dimensional computations vs robotic wing experiments". In: *Journal of Experimental Biology* 207.3, pp. 449–460.

Weymouth, Gabriel D. and Yue, Dick K P (2011). "Boundary data immersion method for Cartesian-grid simulations of fluid-body interaction problems". In: *Journal of Computational Physics* 230.16, pp. 6233–6247.

Xiao, Hong, Febrianto, Eky, Zhang, Qiaoling, and Cirak, Fehmi (2019). "An Immersed Discontinuous Galerkin Method for Compressible Navier-Stokes Equations on Unstructured Meshes". In: *International Journal for Numerical Methods in Fluids*, pp. 1–23.

Xie, Zhihua and Stoesser, Thorsten (2020). "A three-dimensional Cartesian cut-cell/volume-of-fluid method for two-phase flows with moving bodies". In: *Journal of Computational Physics* 416, p. 109536.

Xin, Jianjian, Shi, Fulong, Jin, Qiu, and Lin, Chao (2018). "A radial basis function based ghost cell method with improved mass conservation for complex moving boundary flows". In: *Computers and Fluids* 176, pp. 210–225.

Xu, Lincheng, Tian, Fang Bao, Young, John, and Lai, Joseph C.S. (2018). "A novel geometry-adaptive Cartesian grid based immersed boundary–lattice Boltzmann method for fluid–structure interactions at moderate and high Reynolds numbers". In: *Journal of Computational Physics* 375, pp. 22–56.

Yu, Hang, Pantano, Carlos, and Cirak, Fehmi (2019). "Large-Eddy Simulation of Flow Over Deformable Parachutes using Immersed Boundary and Adaptive Mesh". In: *AIAA Scitech 2019 Forum* January.

Zeng, Xianyi and Farhat, Charbel (2012). "A systematic approach for constructing higher-order immersed boundary and ghost fluid methods for fluid – structure interaction problems". In: *Journal of Computational Physics* 231.7, pp. 2892–2923.

Zheng, Hongyu, Xie, Fangfang, Ji, Tingwei, and Zheng, Yao (2020). "Kinematic parameter optimization of a flapping ellipsoid wing based on the data-informed self-adaptive quasi-steady model". In: *Physics of Fluids* 32.4, p. 041904.

A Gantt Chart

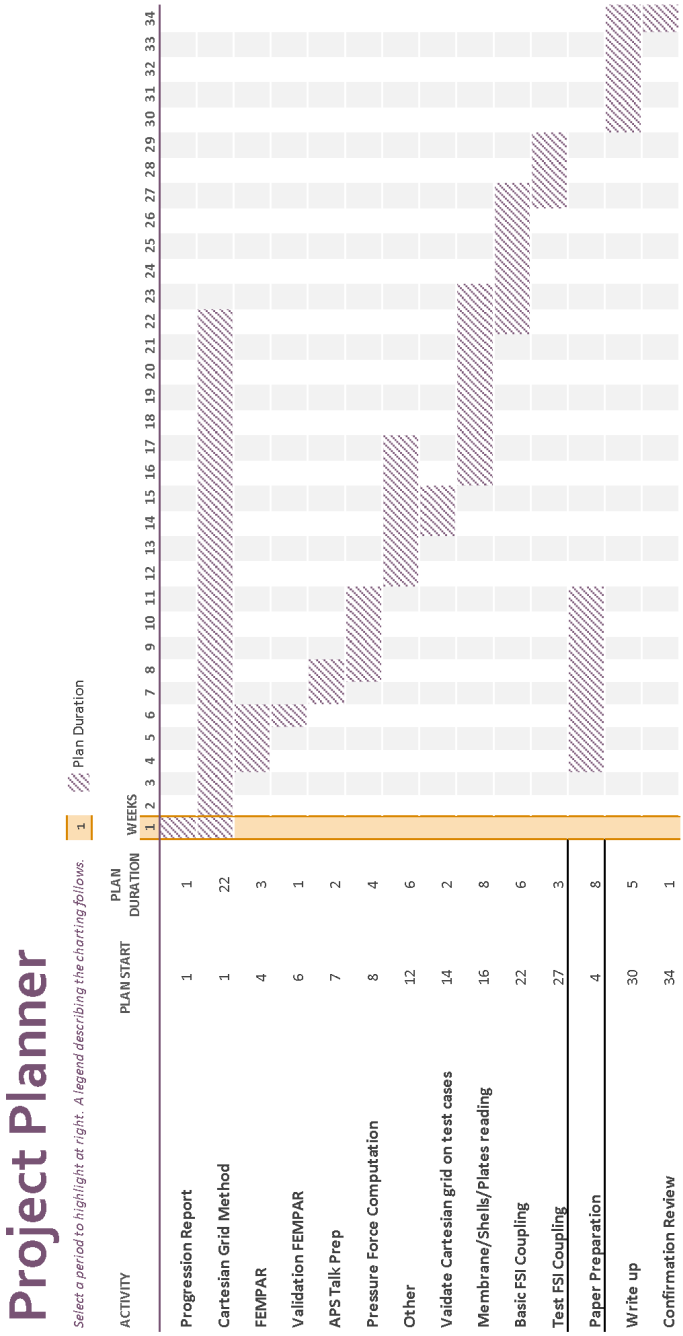

Page left intentionally blank.